DFT studies of the copper active site in AA13 polysaccharide monooxygenases

Chinh N. Le[1], Cuong X. Luu[1], Son Tung Ngo[2, 3], Van V. Vu[1, 4*]

[1]NTT Hi-Tech Institute, Nguyen Tat Thanh University
[2]Laboratory of Theoretical and Computational Biophysics, Ton Duc Thang University
[3]Faculty of Applied Sciences, Ton Duc Thang University
[4]Faculty of Biotechnology, Nguyen Tat Thanh University

Abstract:

AA13 polysaccharide monooxygenases (AA13 PMOs) are novel enzymes that break down starch using a copper active site in a substrate binding groove on a solvent-exposed surface. The structure of the copper active site is influenced by the residues in the groove, while the crystal structure of Cu(II)-AA13 was damaged by photoreduction and lacked two exogenous ligands. We utilized density functional theory (DFT) calculations to obtain insights into the structure of Cu(II)-AA13 in the presence and absence of a key residue (G89) of the groove that interferes with the distal coordination site. Results show that the copper active site of AA13 PMOs can exhibit both 6-coordinate and a 5-coordinate structures depending on position of G89. The active site features are intermediate to those in AA9 and AA10 PMOs, which are the most abundant and well characterized PMO families. In addition, the superoxo species of AA13 has structural parameters halfway between those in AA9 and AA10 PMOs. The structural relationship between the active site and intermediates of AA13 with AA9 and AA10 PMOs is also consistent with their evolutionary relationship.

Keywords: biofuel, DFT calculations, oxygen activation, polysaccharide monooxygenases.

Classification number: 2.1

Introduction

Oxygen activation at the copper active site of PMOs have gained significant attention in the past decade (Fig. 1) [1-9]. This active site is located on a solvent-exposed protein surface (Fig. 1A) in which the copper centre is coordinated by two absolute conserved histidine residues forming a histidine brace on the equatorial coordination plane (Figs. 1B and 1C). The distal site is occupied by a tyrosine residue in some PMO families or by a hydrophobic residue in other PMO families. It is responsible for selective hydroxylation of one of the two C-H bonds of the glycosidic linkage in polysaccharides (Fig. 1D). This hydroxylation is followed by an elimination step leading to the cleavage of the glycosidic linkage. PMOs can work in an endo fashion by creating new chain ends that are accessible by canonical glycoside hydrolases. PMOs can thus significantly boost the activity of glycoside hydrolases in degrading recalcitrant polysaccharides.

Several PMOs families have been reported thus far. Most of these families are active on the β(1→4) glycosidic linkages found in cellulose, hemicellulose, and chitin. AA13 is the only family of PMOs active on α(1→4) glycosidic linkages in starch. There are two major types of starch substrates termed as amylose and amylose pectin. Amylose only contains α(1→4) linkages and forms single and double helices that in turn form a microcrystalline structure. Amylopectin, on the other hand, also contains α(1→6) linkages that form branches. Amylopectin is thus more amorphous and is much
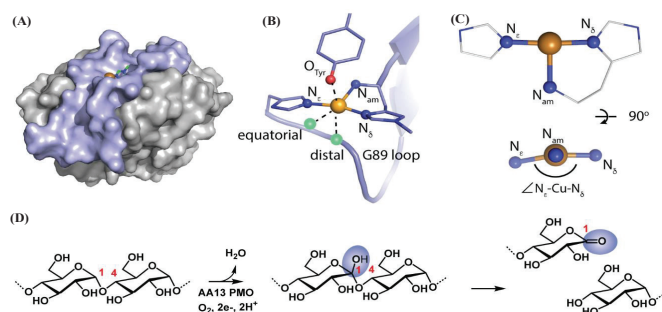

Fig. 1. Structure and reaction of AA13 PMOs. (A) Overall structure of AA13 PMOs with highlighted substrate binding groove and copper active site. **(B)** The copper active site. **(C)** The histidine brace motif. **(D)** Hydroxylation of the C1 position leading glycosidic linkage cleavage.

more amenable to hydrolysis by the canonical glycoside hydrolases (amylases). In contrast, amylose is considered a resistant starch that is digested more slowly by amylases. Recent work has shown that AA13 PMOs are remarkably more active on amylose than on amylopectin [10]. Unlike other PMOs, AA13 PMOs use a shallow surface groove to bind amylose double helices. The active site of AA13 PMOs is modulated by residues in this groove including a flexible loop that could interfere with the distal coordination site (Fig. 1B). In addition, due to the effect of radiation damage during data collection, possibly both equatorial and distal ligands are lacking and the structure of AA13 PMOs in the Cu(II) oxidation

Corresponding author: Email: anhvan.vu@gmail.com

state remains unclear. In this work, we utilized DFT calculations to investigate the active site structure and the influence of the flexible loop on the inner-coordination sphere of Cu(II)-AA13.

Methods

The input structures for AA9 and AA13 PMOs were obtained from the PDB files 5TKI [11] (Fig. 2A) and 4OPB [12] (Fig. 2B), respectively. Residues surrounding the copper centre, which are conserved throughout each family, were taken into account. Water molecules were added to the equatorial (O_{eq}) and distal (O_{dis}) coordination sites of AA13 PMO to create the input structure. Geometries of the species were optimized with the Gaussian 09 package [13] using the B3LYP functional at 6-31g(d) basis set [14] as previously described for PMOs [15, 16]. The solvation model was the dielectric polarized continuum model (D-PCM).
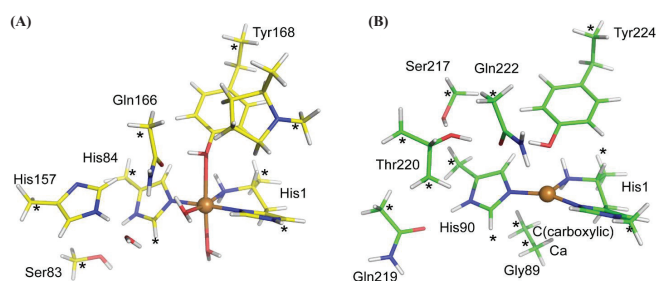

Fig. 2. (A) Starting structures for AA9 (5TKI) and (B) AA13 (PDB ID 4OPB). Asterisks denote frozen atoms during the DFT optimization procedure. The copper centres are shown as orange spheres.

Results and discussion

Effect of permittivity on the DFT calculation results

We initially carried out DFT calculation for the copper active site in NCU01050, a PMO belonging to the AA9 family. This PMO has a very high-resolution structure obtained with both X-ray and neutron diffraction (Fig. 3A). When DFT calculations were carried out in vacuum, the optimized structure deviated significantly from the crystal structure (Table 1 and Fig. 3B). The Cu-O_{Tyr} decreased from 2.683 to 2.360 Å, while the Cu-O_{dis} distance increased from 2.430 to 2.980 Å. The $\angle N_\varepsilon$-Cu-N_δ angle decreased from 178.0° to 164.5° resulting in the distortion of the equatorial plane (Fig. 3A). These three calculated metrics approach experimental values when the calculations were performed in a medium with higher permittivity (diethyl ether, ε=4.33) (Fig. 3C). When carried out in water (ε=80.1), these three calculated metrics
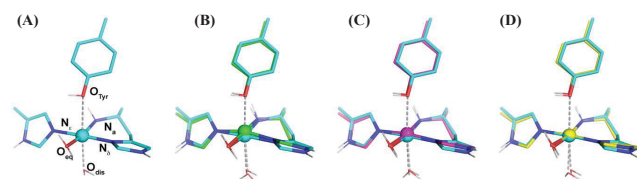

Fig. 3. The coordination structure of the copper active site in an AA9 PMO. (A) The crystal structure of AA9 PMO (5TKI). **(B-D)** DFT structures of AA9 PMO obtained in vacuum, diethyl ether, and water, respectively, overlaid on the crystal structure.

matched experimental values. This result indicates that the medium polarization has strong effect on the DFT calculations of the copper active site in PMOs.

Table 1. The effect of the medium permittivity on DFT calculation results of the copper active site in Cu(II)-AA9 (all distances reported in Å).

NCU01050	Cu-N_δ	Cu-N_ε	Cu-N_{am}	Cu-O_{Tyr}	Cu-O_{eq}	Cu-O_{dis}	$\angle N_\varepsilon$-Cu-N_δ (°)
XRD, 5TKI	1.979	1.974	2.062	2.683	1.981	2.430	178.0
Vacuum, ε=1	1.932	1.923	2.028	2.360	2.074	2.980	164.5
Diethyl ether, ε=4.33	1.924	1.922	2.029	2.569	2.070	2.542	172.5
Water, ε=80.1	1.923	1.929	2.031	2.710	2.064	2.422	177.0

Optimised structures of Cu(II)-AA13

We added two water molecules to the equatorial and distal coordination sites of AA13 to create two input models for Cu(II)-AA13: Model 1 without G89 backbone (Fig. 4A) and Model 2 with G89 backbone (Fig. 4B). DFT optimization was then carried out for these models in vacuum, diethyl ether, and water.
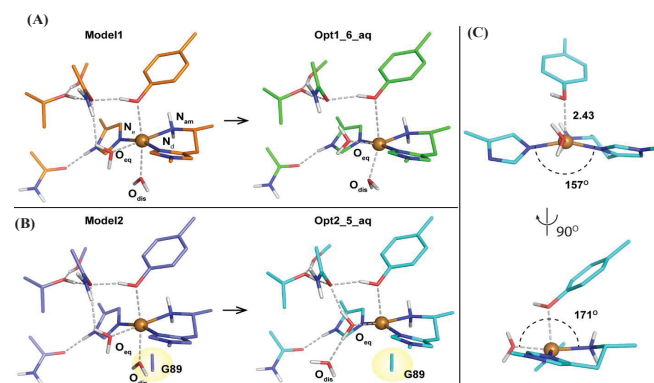

Fig. 4. DFT optimized geometries of the copper active site in AA13. (A) Without G89 backbone. **(B)** With G89 backbone. **(C)** Close-up view of the inner sphere of Opt2_5_aq. Oeq and Odis represent the aqueous ligands added to the equatorial and distal coordination sites in the input structures.

In the absence of the G89 backbone, DFT optimization resulted in a 5-coordinate copper species in vacuum (Opt1_5_vc), and a 6-coordinate copper species in both diethyl ether (Opt1_6_et) and water (Opt1_6_aq) (Table 2). These results indicate that the medium with higher permittivity better stabilizes the distal axial aqueous ligand in AA13 as also observed in the calculations with Cu(II)-AA9 presented above.

Table 2. Structural parameters obtained from DFT optimizations for Cu(II)-AA13 (all distances reported in Å).

	Cu-N_δ	Cu-N_ε	Cu-N_{am}	Cu-O_{Tyr}	Cu-O_{eq}	Cu-O_{dis}	$\angle N_\varepsilon$-Cu-N_δ (°)
Opt1_5_vc	1.959	1.972	2.072	2.358	2.068		155.9
Opt1_6_et	1.941	1.959	2.069	2.823	2.128	2.368	170.8
Opt1_6_aq	1.941	1.958	2.072	2.972	2.137	2.302	173.2
Opt2_5_vc	1.955	1.970	2.080	2.349	2.067		156.2
Opt2_5_et	1.953	1.974	2.081	2.404	2.048		156.1
Opt2_5_aq	1.951	1.979	2.077	2.425	2.029		157.1

In the presence of the G89 backbone, geometry optimization resulted in a 5-coordinate species in all three media investigated, where the distal aqueous ligand was forced out of the binding position. Consequently, the copper centre moved toward the proximal O_{Tyr} ligand resulting in a bent histidine brace (Figs. 4B and 4C). The structural parameters of all 5-coordinate species (Opt1_5_vc, Opt2_6_vc, Opt2_5_et, and Opt2_5_aq) are very similar to one another (Table 2).

Energy difference between 5-coordinate and 6-coordinate copper(II) species in AA13

In vacuum, the optimization of Model1 converged to a 5-coordinate species after a long "lagging" period of about 30 steps (step 20-50) (Fig. 5) in which the copper centre was 6-coordinate. In diethyl ether and water, our calculations stopped at 6-coordinate species and did not optimize any further. We thus took a 5-coordinate intermediate species at step 75 of the optimization in vacuum and further optimized it using the same functional and basis set in diethyl ether and water and obtained two optimized structures, namely, Opt1_5_et and Opt1_6_aq, respectively. This allowed us to compare single point energies of 5-coordinate and 6-coordinate species (Table 3). The energy difference between the 5-coordinate species and 6-coordinate species decreases as the dielectric constant of the medium increases. Nevertheless, the energy difference between the 5- and 6-coordinate species in water is significantly large (~-2.9 kcal/mol). This result indicates that 5-cooridnate species is likely preferred by Cu(II)-AA13 PMOs.
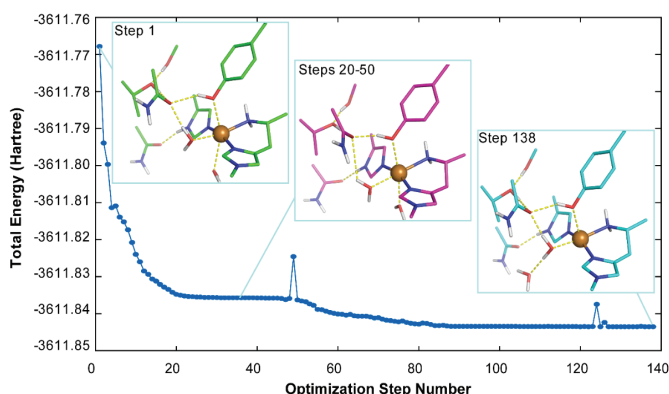

Fig. 5. DFT optimization process of Model 1 in vacuum.

Table 3. Energy difference between 5- and 6-coordinate species obtained with single point energy calculation.

Medium	ε	5-coordinate (Hartree)	6-coordinate (Hartree)	Energy difference (Hartree)	Energy difference (kcal/mol)
Vacuum*	1	-3612.65626130	-3612.64819820	-0.00806310	-5.06
Diethyl ether	~4.33	-3612.80146385	-3612.79488220	-0.00658156	-4.13
Water	~80.1	-3612.84860538	-3612.84397050	-0.00463488	-2.91

*6-coordinate species in vacuum was taken at the optimization step 50.

Optimized structure of a key intermediate of AA13 PMOs

One of the first key intermediates of the PMO reaction is the O_2-adduct, namely, a Cu(II)-superoxo intermediate. We carried out DFT calculations for Cu(II)-AA13-superoxo in the presence of G89 and absence of O_{dis}. Both singlet and triplet spin states were investigated. The optimized structures of these two states overlay well with one another (Fig. 6). The optimized structural parameters are presented in Table 4. These parameters are similar to one another although Cu-O_{Tyr} and ∠Nε-Cu-Nδ change slightly as observed for Cu(II)-AA9. Single point energy was also calculated for Cu(II)-AA13-superoxo (Table 5). The triplet state is remarkably more stable than the singlet state (-19 kcal/mol), which is consistent with the literature [15, 16].
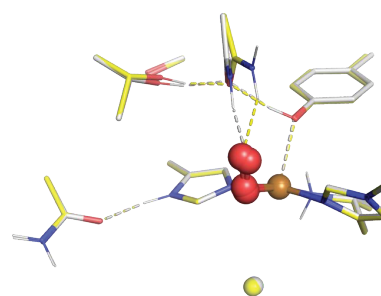

Fig. 6. Overlaid optimized structures of Cu(II)-AA13-superoxo intermediate in singlet (carbon atoms shown as white sticks) and triplet (carbon atoms shown as yellow sticks) spin states.

Table 4. Structural parameters obtained from DFT optimizations for Cu(II)-AA13-superoxo (all distances reported in Å).

	Cu-N_δ	Cu-N_ε	Cu-Na	Cu-O_{Tyr}	Cu-$O1_{oo}$	Cu-$O2_{oo}$	∠Nε-Cu-N_δ (°)
OptO2_S_vc	1.941	1.957	2.137	2.442	1.892	2.762	163.6
OptO2_S_et	1.93	1.955	2.126	2.487	1.888	2.760	166.8
OptO2_S_aq	1.927	1.959	2.114	2.509	1.886	2.768	167.5
OptO2_T_vc	1.967	1.977	2.134	2.378	1.981	2.913	158.7
OptO2_T_et	1.957	1.974	2.128	2.413	1.987	2.915	161.7
OptO2_T_aq	1.954	1.978	2.119	2.423	1.990	2.917	162.2

Table 5. Energy difference between triplet and singlet states of Cu(II)-AA13-superoxo obtained with single point energy calculation.

Medium	ε	Singlet (Hartree)	Triplet (Hartree)	Energy difference (Hartree)	Energy difference (kcal/mol)
Vacuum	1	-3690.1971719	-3690.2276186	-0.0304467	-19.11
Diethyl ether	~4.33	-3690.2462955	-3690.2766351	-0.0303396	-19.04
Water	~80.1	-3690.2652720	-3690.2957090	-0.0304370	-19.10

Implication in the evolution of PMOs

The structures of Cu(II)-AA13 and Cu(II)-AA13-superoxo correlate well with the phylogenetic relationship of AA13 with AA10 and AA9 PMOs, which are the two most abundant and well characterized PMO families. Phylogenetic analysis showed that

the AA13 clade is placed between the AA9 and AA10 clades (Fig. 7) [17]. Cu(II)-AA9 has an elongated octahedral copper centre, while Cu(II)-AA10 has a trigonal bipyramidal copper centre (Fig. 7A) [17]. The copper centre in Cu(II)-AA13 exhibit both 5- and 6-coordinate features, in which the 5-coordinate structure is preferred. This 5-coordinate structure is halfway between those in AA9 and AA10.

In addition, the O_2 moiety in the Cu(II)-AA9-O_2 intermediate binds in an end-on mode with the terminal O atom pointing down the distal space forming H-bonds with a water molecule and two outer sphere residues (PDB ID 5TKH) (Fig. 7B) [11]. On the other hand, the O_2 moiety of the Cu(II)-AA10-O_2 intermediate binds in a bidentate mode with the terminal O atom oriented toward the proximal space (PDB ID 5VG0) [18]. The O_2 moiety of Cu(II)-AA13-O_2 binds in an end-on mode, but, unlike in AA9, the terminal O atom is oriented toward the proximal space. This binding configuration is also halfway between the superoxo intermediate in AA9 and AA10 PMOs. These results show that as the PMO family evolved, the active site structure and key reaction intermediates also gradually changed.
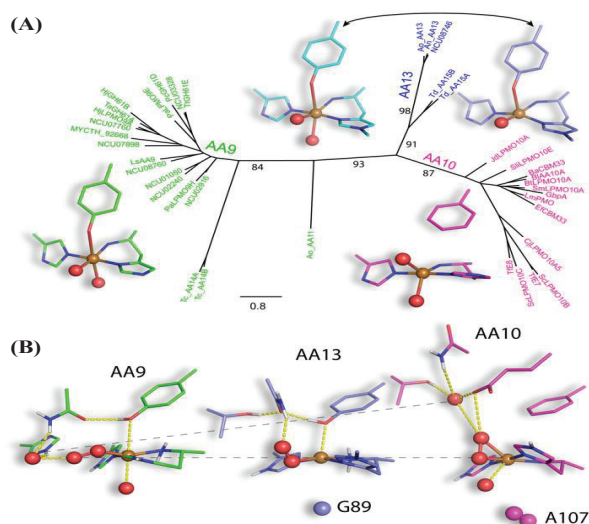

Fig. 7. The relationship between the copper active sites in PMO families. (A) The phylogenetic tree of structurally characterized PMOs. The active site core structures are shown for AA9, AA10, and AA13 PMOs. **(B)** Comparison of the structure of the dioxygen intermediate of AA13 (derived with DFT) with the crystal structures of those in AA9 (5TKH) and AA10 (5VG0).

Conclusions

The copper(II) active site of AA13 PMOs and their superoxo intermediates were optimized for the first time. The preferred structure of Cu(II)-AA13 is a distorted 5-coordinate species. This structure is halfway between those of the most abundant and well characterized AA9 and AA10 PMO families. Likewise, the structure of the superoxo intermediate is also halfway between that of an end-on intermediate in AA9 PMOs and a side-on intermediate in AA10 PMOs. The structural features of AA13 are consistent with their evolutionary relationship with AA9 and AA10 PMOs.

COMPETING INTERESTS

The authors declare that there is no conflict of interest regarding the publication of this article.

RERERENCES

[1] G.V. Kolstad, et. al (2010), "An oxidative enzyme boosting the enzymatic conversion of recalcitrant polysaccharides", *Science*, **330(6001)**, pp.219-222.

[2] P.V. Harris, et al. (2010), "Stimulation of lignocellulosic biomass hydrolysis by proteins of glycoside hydrolase family 61: Structure and function of a large, enigmatic family", *Biochemistry*, **49(15)**, pp.3305-3316.

[3] W.T. Beeson, C.M. Phillips, J.H.D. Cate, M.A. Marletta (2012), "Oxidative cleavage of cellulose by fungal copper-dependent polysaccharide monooxygenases", *J. Am. Chem. Soc.*, **134(2)**, pp.890-892.

[4] C.M. Phillips, W.T. Beeson, J.H.D. Cate, M.A. Marletta (2011), "Cellobiose dehydrogenase and a copper-dependent polysaccharide monooxygenase potentiate cellulose degradation by neurospora crassa", *ACS Chem. Biol.*, **6(12)**, pp.1399-1406.

[5] R.J. Quinlan, et al. (2011), "Insights into the oxidative degradation of cellulose by a copper metalloenzyme that exploits biomass components", *PNAS*, **108(37)**, pp.15079-15084.

[6] V.V. Vu, et al. (2014), "A family of starch-active polysacchride monooxygenases", *PNAS*, **111(38)**, pp.13822-13827.

[7] G.R. Hemsworth, B. Henrissat, G.J. Davies, P.H. Walton (2014), "Discovery and characterization of a new family of lytic polysaccharide monooxygenases", *Nat. Chem. Biol.*, **10(2)**, pp.122-126.

[8] F. Sabbadin, et al. (2018), "An ancient family of lytic polysaccharide monooxygenases with roles in arthropod development and biomass digestion", *Nat. Comm.*, **9(1)**, DOI: 10.1038/s41467-018-03142-x.

[9] M. Couturier, et al. (2018), "Lytic xylan oxidases from wood-decay fungi unlock biomass degradation", *Nat. Chem. Biol.*, **14**, pp.306-310.

[10] V.V. Vu, et al. (2019), "Substrate selectivity in starch polysaccharide monooxygenases", *Journal of Biological Chemistry*, **294(32)**, pp.12157-12166.

[11] W.B. O'Dell, P.K. Agarwal, F. Meilleur (2017), "Oxygen activation at the active site of a fungal lytic polysaccharide monooxygenase", *Angew. Chem. Intl. Ed.*, **56(3)**, pp.767-770.

[12] L.L. Leggio, et al. (2015), "Structure and boosting activity of a starch-degrading lytic polysaccharide monooxygenase", *Nat. Commun.*, **6**, DOI: 10.1038/ncomms6961.

[13] https://gaussian.com/citation/.

[14] C.I. Bayly, P. Cieplak, W. Cornell, P.A. Kollman (1993), "A well-behaved electrostatic potential based method using charge restraints for deriving atomic charges: The RESP model", *The Journal of Physical Chemistry*, **97(40)**, pp.10269-10280.

[15] S. Kim, J. Ståhlberg, M. Sandgren, R.S. Paton, G.T. Beckham (2014), "Quantum mechanical calculations suggest that lytic polysaccharide monooxygenases use a copper-oxyl, oxygen-rebound mechanism", *PNAS*, **111(1)**, pp.149-154.

[16] C.H. Kjaergaard (2014), "Spectroscopic and computational insight into the activation of O_2 by the mononuclear Cu centre in polysaccharide monooxygenases", *PNAS*, **111(24)**, pp.8797-8802.

[17] V.V. Vu, S.T. Ngo (2018), "Copper active site in polysaccharide monooxygenases", *Coord. Chem. Rev.*, **368**, pp.134-157.

[18] J.P. Bacik, et al. (2017), "Neutron and atomic resolution X-ray structures of a lytic polysaccharide monooxygenase reveal copper-mediated dioxygen binding and evidence for N-terminal deprotonation", *Biochemistry*, **56(20)**, pp.2529-2532.